Atmos. Meas. Tech. Discuss., 6, 10511–10550, 2013
www.atmos-meas-tech-discuss.net/6/10511/2013/
doi:10.5194/amtd-6-10511-2013

Atmospheric Measurement Techniques Discussions

Retrieving aerosol height from the oxygen A band: a fast forward operator and sensitivity study concerning spectral resolution, instrumental noise, and surface inhomogeneity

A. Hollstein and J. Fischer

Institute for Space Sciences, Freie Universität Berlin, Department of Earth Sciences, Germany

Received: 6 November 2013 – Accepted: 21 November 2013 – Published: 5 December 2013

Correspondence to: A. Hollstein (andre.hollstein@fu-berlin.de)

Published by Copernicus Publications on behalf of the European Geosciences Union.

Abstract

Hyperspectral radiance measurements in the oxygen A band are sensitive to the vertical distribution of atmospheric scatterers, which in principle allows to retrieve aerosol height from future instruments like TROPOMI, OCO2, FLEX, and CarbonSat. Discussed in this paper is a fast and flexible forward operator for the simulation of hyperspectral radiances in the oxygen A band and, based on this scheme, a sensitivity study about the inversion quality of aerosol optical thickness, aerosol mean height, and aerosol type. The forward operator is based on a lookup table with efficient data compression based on principal component analysis. Linear interpolation and computation of partial derivatives is performed in the much smaller space of expansion coefficients rather then wavelength. Thus, this approach is computationally fast and at the same time memory efficient. The sensitivity study explores the impact of instrument design on the retrieval of aerosol optical thickness and aerosol height. Considered are signal to noise ratio, spectral resolution, and spectral sampling. Also taken into account are surface inhomogeneities and variations of the aerosol type.

1 Introduction

Multiple fields of research can benefit from an accurate and reliable aerosol height product. Among others are atmospheric sciences, where aerosol vertical distribution and interaction with clouds and radiation is discussed (e.g. Chin et al., 2009; Lohmann and Feichter, 2005) as well as long range aerosol transport (e.g. Betzer et al., 1988; Andreae, 1983) and source attribution (e.g. McConnell et al., 2007; Clarke and Noone, 1985), human health (e.g. Nel, 2005; Harrison and Yin, 2000; Seaton et al., 1995) and pollution studies (e.g. McMichael et al., 2003; Pöschl, 2005), and in remote sensing of the atmosphere, where its effect on the retrieval of total aerosol optical thickness is discussed (e.g. Quijano et al., 2000; Duforêt et al., 2007; McClain, 2009; Muller et al., 2007).

AMTD
6, 10511–10550, 2013

LIDAR measurements (e.g. using EARLINET Amodeo et al., 2007), airborne experiments (e.g. Zieger et al., 2007), or balloon ascends (e.g. Rosen et al., 1975) can be used to derive aerosol vertical profiles on local scales, while the backscatter LIDAR CALIOP onboard the satellite CALIPSO (Winker et al., 2009) is currently the only instrument which provides information on a global scale. A limitation of CALIPSO measurements is their sparse spatial and temporal resolution (Winker et al., 2010; Amiridis et al., 2013), which could be improved drastically by deriving aerosol height directly from passive imaging instruments.

Attempts to use the oxygen absorption bands for an aerosol height retrieval (e.g. Gabella et al., 1999; Koppers et al., 1997; Corradini and Cervino, 2006; Pelletier et al., 2008; Sanghavi et al., 2012; Frankenberg et al., 2012; Kokhanovsky and Rozanov, 2010) or cloud top height retrieval (e.g. Heidinger and Stephens, 2000; Preusker and Lindstrot, 2009; Fischer and Grassl, 1991; Rozanov and Kokhanovsky, 2004) have been published in the past. For a case study, Dubuisson et al. (2009) and Duforêt et al. (2007) exploited MERIS and POLDER data to derive aerosol height over oceans from reflectance ratios of channels inside and outside the O_2A band. Sanghavi et al. (2012) discussed to use the O_2A and O_2B band to derive aerosol vertical distribution from SCIAMACHY data and applied the technique to a scene above Kanpur (India). For aerosols over land no operational data product exists to our knowledge, although hyperspectral measurements within the oxygen A band were and are performed by operational instruments such as SCIAMACHY, GOSAT, GOME, and GOME2. However, it is possible to derive the absorbing aerosol index (Torres et al., 1998; De Graaf et al., 2005) from such type of instruments, which is among other aerosol parameters also sensitive to aerosol height, but does not retrieve quantitative aerosol vertical distribution parameters.

In the near and not too distant future, hyperspectral measurements within the oxygen A band will become widely available from instruments such as OCO2 (Haring et al., 2004; Crisp and Johnson, 2005), TROPOMI (Veefkind et al., 2012), Sentinel-4 (ESA, 2012), Sentinel-5 (ESA, 2012), or if selected, ESA Earth Explorer (Bézy et al., 2008;

AMTD
6, 10511–10550, 2013

Meijer et al., 2012) missions like FLEX (Clissold, 2008; Rascher et al., 2008; Stoll, 2003) or CarbonSat (Velazco et al., 2011). Operational aerosol height products are at least planed for TROPOMI onboard the Sentinel 5 precursor (Veefkind et al., 2012; Sanders and de Haan, 2013) and for the Sentinels 4 and 5 (ESA, 2012). The aim of these products is to distinguish between aerosols in the planetary boundary layer and the free troposphere with desirably estimation of aerosol type, e.g. to constrain surface concentrations of particulate mater (ESA, 2012). The specifications of these instruments vary widely with respect to spectral resolution, spatial resolution, temporal resolution, and signal to noise ratio (SNR); and all mission design parameters might have an impact on a possible retrieval of aerosol height.

Sanders and de Haan (2013) discussed the possible retrieval accuracy of aerosol height by propagating measurement and a priori errors trough a locally linearized radiative transfer model using the framework of optimal estimation by Rodgers (2000). From the perspective of an operational retrieval, a positive result for the retrieval error with respect to given user requirements fulfills only a necessary condition. A real world retrieval must in addition converge robustly, treat multiple minima in the used cost function, deal with deviation of the real and the model atmosphere, and needs to be computationally fast enough to process and possibly reprocess large amounts of hyperspectral radiance data.

Aim of this paper is to propose and present a fast and efficient forward operator based on accurate radiative transfer simulations. It was applied in a simple inversion scheme, which can represent a generic real world retrieval algorithm. The forward operator is based on a lookup table with efficient data compression based on a principal component analysis. Linear interpolation and computation of partial derivatives is performed in the much smaller space of expansion coefficients, which makes this approach computationally fast and at the same time memory efficient.

The fast forward operator is described in Sect. 2 while Sects. 3 and 4 cover the setup of the sensitivity study and the inversion scheme. The applied instrument error model is described in Sect. 5 and the results of the sensitivity study are discussed in Sect. 6.

AMTD
6, 10511–10550, 2013

2 Fast forward operator

The following discussion is based on the assumption, that the inversion of radiative transfer simulations for a complex atmosphere is the most suitable path to retrieve aerosol height. Radiative transfer simulations numerically map an atmospheric state, which includes the quantities of interest, with simulated measurements. An inversion operator, which could include additional prior knowledge is then used as retrieval. This assumption is emphasized, since this approach requires in general complex modeling, is prone to errors, requires precise knowledge about the optical properties of the atmosphere, the surface, and the aerosols, and can be computationally very demanding. To our best knowledge, no simpler approach exists up to now, as it was found e.g. for fluorescence emitted by vegetation, which can be retrieved using Fraunhofer lines without relying on radiative transfer (e.g. Frankenberg et al., 2011; Joiner et al., 2011).

The design of the fast forward operator was mainly driven by considerations about computational speed on standard computer hardware and simulation accuracy. This leads either to the use of the radiative transfer model directly as forward model (e.g. compare the OCO2 retrieval by Bösch et al., 2006), or to use the classical approach of a forward operator based on interpolation within a lookup table populated by radiative transfer calculations. The following discussion could also be based on neural networks, but the interpolation approach was chosen since its behavior is easier to understand and does not depend on tuned neural network parameters.

Using a full scale radiative transfer model as forward operator entails some inherent advantages, as one does not rely on (linear) interpolation, which can introduce errors due to the locally nonlinear behavior of solutions of the radiative transfer equation. However, this approach will always be much more demanding computationally as a simple lookup table interpolation and thus might be unsuitable for applications on standard computer hardware systems. A possible solution is to speed up the radiative transfer, which in general sacrifices simulation accuracy, which could cancel some of the advantages of this approach. On the other hand, populating a high dimensional lookup table

AMTD
6, 10511–10550, 2013

with hyperspectral radiative transfer simulations is computationally expensive. However, for the case of the oxygen A band, this obstacle can be lifted by exploiting the high correlation of the spectrum with respect to variations of the atmospheric state. Natraj et al. (2005) were using principal component analysis to speed up the calculation of optical parameters for a radiative transfer model, while Hollstein and Lindstrot (2013) have presented an approach based on principal component analyses which can speed up the population of the lookup table by one or more orders of magnitude. Following the latter approach, a higher speedup is achieved for larger lookup tables. Hence, the computational aspect of filling up a potentially large lookup table can be considered as very well under control.

To summarize this approach: it was shown explicitly for the oxygen A band, that a comparably small, randomly selected subset of spectra is sufficient to compute a set of principal components, which can be used to reconstruct the total lookup table, where the reconstruction accuracy is a function of the randomly selected subset of spectra and the number of used principal components. Then, Hollstein and Lindstrot (2013) presented an algorithm, which makes it possible to compute the expansion coefficients of a certain spectrum by simulating only a small subset of spectral channels. This implies, that for the oxygen A band, a relatively small number of spectral channels is sufficient to reconstruct the hyperspectral simulation, thus leading to an enormous speedup. This approach makes it feasible to increase the allowed computation time of the radiative transfer, e.g. to increase simulation accuracy by using higher vertical and spatial resolution or by taking 3-D effects into account.

Next to populating the lookup table, its possible huge size can become a major obstacle, especially for hyperspectral applications. As a consequence, the proposed fast forward operator is also based on principal component analysis. In this way, effective data compression is used to reduce the size of the lookup table and also to gain computational speedups for the interpolation within that table.

The approach consists of two tables, one which stores the expansion coefficients of the simulated spectra with respect to the corresponding atmospheric state and

AMTD
6, 10511–10550, 2013

a second one for the used principal components. Formally: let $\boldsymbol{x} \in \mathbb{R}^{n_x}$ be a state vector with n_x free parameters for the radiative transfer model $\mathrm{RT}(\boldsymbol{x}) = \boldsymbol{y} \in \mathbb{R}^{n_\lambda}$, where $\boldsymbol{y}$ is the simulated spectrum and n_λ is the number of simulated spectral channels. A generic lookup table would then consists of a possibly large set with n states: $X = (\boldsymbol{x}_1, \ldots, \boldsymbol{x}_n)$ and a related set of simulated spectra $Y = (\boldsymbol{y}_1, \ldots, \boldsymbol{y}_n)$. Principal component analysis can be used to derive a number of $n_p \ll n$ principal components $\boldsymbol{p}_i \in \mathbb{R}^{n_\lambda}, i = 1, \ldots, n_p$, which can be combined in the principal component matrix $\mathbf{P}_{n_p} \in \mathbb{R}^{n_P \times n_\lambda}$ with $[\mathbf{P}_{n_p}]_{ij} = [\boldsymbol{p}_i]_j$. The expansion coefficients for each spectrum $\boldsymbol{c}_i = \mathbf{P} \times \boldsymbol{y}_i, i = 1, \ldots, n$ can be computed such that a reconstructed spectrum $\tilde{\boldsymbol{y}}_i$ can be expressed as $\tilde{\boldsymbol{y}}_i = \mathbf{P}^{-1} \times \boldsymbol{c}_i = \mathbf{P}^{\mathrm{T}} \times \boldsymbol{c}_i$. The matrix $\mathbf{P}_{n_P}$ is orthogonal since the p_i are pairwise orthogonal, such that $\mathbf{P}^{-1} = \mathbf{P}^{\mathrm{T}}$. The reconstruction residual $\epsilon_i = |\boldsymbol{y}_i - \tilde{\boldsymbol{y}}_i|, i = 1, \ldots, n$ for a single spectrum y_i generally depends on the number of principal components and the reconstructed spectrum, while the mean reconstruction residual with respect to the total lookup table $\epsilon = \mathrm{mean}(\epsilon_1, \ldots, \epsilon_n)$ only depends on the number of principal components.

In general and with proper computation of $\mathbf{P}_{n_P}$, both residuals are strongly decreasing with increasing number of principal components, thus n_P can be chosen such that the mean reconstruction error is sufficiently smaller then the measurement error of a possible instrument. As a result, the large table Y, which contains simulated spectra can be replaced by the principal component matrix $\mathbf{P}_{n_P}$ and a table $C = (\boldsymbol{c}_1, \ldots, \boldsymbol{c}_{n_l})$ with $\boldsymbol{c}_i = \mathbf{P}_{n_P} \times \boldsymbol{y}_i$, which contains only the expansion coefficients for each spectrum and is by a compression factor n_λ / n_p smaller than Y.

To save large amounts of computation time, the $\boldsymbol{c}_i$ could be computed using the approach presented by Hollstein and Lindstrot (2013). The lookup table C should be small enough to fit easily in the main memory of modern PCs. Not only does this approach save main memory when compared with an uncompressed table, it also saves much computation time since the interpolation and computation of partial derivatives can be computed in the space spanned by the expansion coefficients. This is possible since

AMTD
6, 10511–10550, 2013

the compression from the principal component analysis is linear, thus compression and interpolation can be interchanged.

An interpolation scheme $IT(X, C, \boldsymbol{x}) = \boldsymbol{c}$ in the expansion coefficient space must be implemented from which the desired interpolated spectrum can be computed by multiplying with the principal component matrix:

$$\boldsymbol{y}(\boldsymbol{x}) = \mathbf{P}^{\mathrm{T}}_{n_P} \times \mathrm{IT}(X, C, \boldsymbol{x}). \quad (1)$$

This approach can be implemented to be computationally efficient and enables a simple path to exploit computation on modern GPGPUs. In an initialization step, the lookup table C must be copied to the memory of the GPGPU, which is the slowest part, then very little data transfer is needed since for a single interpolation only the two small vectors $\boldsymbol{x}$ and $\boldsymbol{c}$ need to be transferred from and to the main memory, where the final expansion to the desired spectra could be computed. The spectral resolution of the simulations can be adjusted easily and with little extra computational cost. When the simulations were performed with adequate spectral resolution, it is sufficient to convolve the principal components with the desired response functions to set up the forward operator for a different instrument. This is numerically cheap and can be performed on the fly when the program is called. Similarly, spectral shifts as they occur e.g. for TANSO-FTS onboard GOSAT can be corrected by convolving the principal components with response functions which take the spectral shift into account. Further speedup in an inversion scheme can be achieved by selecting the number of used principal components with respect to the current value of the cost function. In the first steps of an iterative optimization scheme, it might be sufficient to reconstruct the spectra using only a few principal components, since it is sufficient to keep the reconstruction error well below the difference of actual measurement and simulation. The number of principal components can then be increased with decreasing cost function value to improve the reconstruction quality.

AMTD
6, 10511–10550, 2013

3 Synthetic study setup

Radiative transfer simulations were performed using the MOMO radiative transfer model (see Fell and Fischer, 2001; Hollstein and Fischer, 2012) which is a matrix operator model widely used at *Freie Universität Berlin*. Gaseous absorption was computed using line parameters from the HITRAN spectral database (Rothman et al., 2009) and a modified scheme to compute the k-distribution (Bennartz and Fischer, 2000). The parameter grid for the lookup table is shown in Table 1. The variation of the atmospheric state includes surface pressure, aerosol optical thickness, aerosol mean height, aerosol type, surface reflectance, and the viewing geometry. The surface reflectance spectrum is assumed to be a linear function and is modeled using a reflectance value at 755 nm and at 780 nm. The normalized aerosol vertical distribution $v(h,\mu,\sigma)$ with respect to height above the surface h and mean height μ is modeled using a log normal distribution with a width parameter of $\sigma = 1.1$, which represents a narrow layer-like distribution:

$$v(h,\mu,\sigma) = \frac{1}{h \cdot \log(\sigma)} \exp\left(-\frac{(\log(h) - \log(\mu))^2}{2\log(\sigma)^2}\right). \quad (2)$$

As a result of this setup, the analysis is based on the retrieval of a single aerosol layer when only a single aerosol layer is present. A constant temperature profile is assumed throughout this discussion, since the actual profile should be given as background information. Introducing the temperature profile into this framework poses no specific difficulties and could be easily implemented as proposed by Lindstrot and Preusker (2012).

Several randomly selected spectra at three spectral resolutions are shown in Fig. 1. All spectra within the lookup table were fully simulated and could be used to compute the principal components, as well as evaluating the reconstruction performance for a specific set of principal components. The principal component algorithm provided by the Python package Scikit-learn (Pedregosa et al., 2011) was used to compute the

AMTD
6, 10511–10550, 2013

actual components. The first six components are shown in Fig. 2. Although it is in general unclear how to attribute specific physical properties to a single component, the first two components show a clear signature of the general oxygen absorption features and the linear model of the surface reflectance.

The uncompressed lookup table contains 2 496 000 spectra, each with 4501 channels, which is too large to efficiently compute principal components. As shown by Hollstein and Lindstrot (2013), this is not necessary, since a randomly selected sub sample of spectra of sufficient size is feasible to compute principal components which are valid for the complete lookup table. Since all spectra were fully simulated, it is possible to test the reconstruction accuracy of the total dataset with respect to the number of used principal components.

Figure 3 shows the dependency of the mean of the synthetic signal to noise ratio for the whole lookup table with respect to the number of used principal components. The synthetic signal to noise level was defined as:

$$\mathrm{SNR} = \mathrm{mean}(\boldsymbol{y}_i)/\mathrm{stdev}(\boldsymbol{y}_i - \tilde{\boldsymbol{y}}_i), \tag{3}$$

and is used as measure throughout this paper. The results show clearly, that the reconstruction quality increases strongly with increasing number of principal components. Also, that a number of ten principal components is sufficient to represent the original data with a mean synthetic SNR of approximately 1000.

Histograms of the reconstruction error for increasing values of n_P are shown in Fig. 4. The results clearly show that the reconstruction quality increases dramatically with increasing number of principal components. The histogram for 15 principal components shows a peculiar dip in the middle of the distribution, which sets this distribution slightly apart from the other ones, but causes no difficulties since the whole distribution shows a much better mean reconstruction quality than when using only five principal components. This effect shows that it is in principle difficult to establish a physical link between a principal component and its effect on the overall reconstruction accuracy when it is added to the reconstruction matrix.

AMTD
6, 10511–10550, 2013

The aerosol optical models were implemented according to Levy et al. (2007). These models are also used by the MODIS aerosol retrieval and were specifically designed to fit observations for different locations on the globe. From the published optical properties, the urban, neutral, dust, continental, and absorbing types were implemented and Mie calculations using the implementation provided by Wiscombe (1980) were used to compute phase functions, extinction, and single scattering albedo. Aerosol phase functions at 774.5 nm with respect to scattering angle and optical thickness are shown in Fig. 5.

The approach of this study is to expand on the retrieval error analysis as presented by Sanders and de Haan (2013) and to implement a real world retrieval scheme, where simulated measurements with realistic random errors are fitted using the fast forward operator. This approach is suited to realistically discuss the difficulties which can arise from multiple minima in the cost function, which can be caused by almost linearly dependent partial derivatives of the forward operator.

The dependency of the partial derivative of the forward operator with respect to aerosol optical thickness and aerosol height is shown in Fig. 6 and for surface reflectance and aerosol optical thickness in Fig. 7. The partial derivatives were rescaled with a specific decimal power and corresponding unit, such that both rescaled spectra carry the unit radiance and are of comparable magnitude. By neglecting non-linearity, one can interpret the scaling factors as the specific quantity for both compared parameters, which causes a similar radiance change.

Figure 6 shows the partial derivatives with respect to aerosol height and aerosol optical thickness, which rather strongly depend on the aerosol model and can be largely described by almost linear sections with alternating signs of the slope. This behavior could potentially lead to multiple minima in the least squares cost function. But, their differences could help to discriminate between aerosol types. Figure 7 shows that the partial derivatives with respect to aerosol optical thickness and surface reflectivity are strongly linearly correlated, with a strong dependency on aerosol type. This indicates one of the main theoretical problems with deriving the aerosol height from the oxygen

AMTD
6, 10511–10550, 2013

A band alone. Crucial for the retrieval accuracy will be the proper discrimination of surface reflectivity and aerosol optical depth. Both parameters are highly variable in space and time on short scales, such that prior knowledge with sufficiently small uncertainty will likely be unavailable.

4 Inversion scheme

The fast forward operator was implemented in FORTRAN, parallelized using OpenMP, and run on a standard desktop computer with 8 GB of main memory and an Intel i7-3770 CPU with 4 cores running at 3.2 GHz. The linear interpolation was implemented in FORTRAN such that the Jacobean of the interpolated function is computed analytically without much computational overhead. Results for a simple benchmark are shown in Table 2. Each benchmark result is based on the computation of 50 000 randomly selected states. The benchmark shows that the run time of the forward operator is almost independent from spectral resolution and sublinearly increases with increasing number of principal components.

The Levenberg Marquardt optimization routine *lmder* from the MINIPACK project provided by Moré et al. (1984) was used to minimize the sum of least squares between simulated measurements and results of the fast forward operator. As discussed in Sect. 3, no prior knowledge is assumed since for the crucial variables aerosol type, aerosol height, aerosol optical thickness, and surface reflectance, prior knowledge will likely not be available with sufficiently small error.

The *lmder* routine is implemented for an unbounded problem. To ensure that the search range stays within the bounds of the lookup table, the computed next iteration step was modified such that the bounds of the lookup table can only be reached asymptotically. The modification replaces the computed stepsize to half of the distance between the actual position and the boundary. A certain minimum step size for aerosol optical depth was chosen as convergence criterion for the iteration.

AMTD
6, 10511–10550, 2013

5 Noise model

Scope of this paper is the simulation of general hyperspectral radiometers with arbitrary spectral resolution, spectral sampling, and signal to noise level. As generic noise model, a random noise vector $\boldsymbol{n}$ was added to a forward operator simulation to produce a synthetic measurement $\boldsymbol{y}_m$:

$$\boldsymbol{y}_m = \boldsymbol{y} + \boldsymbol{n}(\boldsymbol{y}), \quad \boldsymbol{n}(\boldsymbol{y}) = \boldsymbol{r}_{-1,1}\text{mean}(\boldsymbol{y})/\text{SNR}, \tag{4}$$

where $\boldsymbol{r}_{-1,1}$ is a vector with the dimension of the simulations which contains random numbers between −1 and 1 and SNR is the prescribed signal to noise ratio. With this definition, the synthetic SNR of a spectral fit is approximately the prescribed SNR number.

Although this is a very simple noise model, it is sufficiently close to a realistic noise model (e.g. see Aiazzi et al., 2006) and avoids the problem of almost zero relative error for small measurements when using pure multiplicative noise.

6 Synthetic retrieval results

The sensitivity study is based on a Monte Carlo approach. A number of 5000 retrievals with randomly selected state vectors is performed for a given setting of spectral resolution, spectral sampling, signal to noise ratio, prior aerosol type information, and surface inhomogeneity. Surface inhomogeneity is modeled by applying the independent column approach, where the mean value over $N_\alpha = 9$ simulations using a range of different surface reflectances is taken. The resulting set of prescribed state vectors and inversion results is then analyzed by means of scatter plots and mean values.

Two named cases are distinguished throughout the analysis, the *best case* and the *realistic case* scenario. The *best case* scenario is characterized by a retrieval with known aerosol type and simulations with homogeneous surface reflectance, while for

AMTD
6, 10511–10550, 2013

the *realistic case* the aerosol type is a free inversion parameter and surface inhomogeneity is taken into account. The two cases can be used to study the effect of an unknown aerosol type, which is believed to have only minor effects (compare Sanders and de Haan, 2013), and also the effect of the finite spatial resolution of a hypothetical sensor. In general, spectral resolution, spectral sampling, and spatial resolution are competing factors for an instrument with given external constraints. Increasing the spectral resolution decreases the amount of energy within each channel, which can be compensated with more sensitive detectors, longer integration time, or a larger footprint on the surface of the Earth. The *realistic case* is therefore more realistic for hyperspectral instruments such as TROPOMI or TANSO-FTS, where an instrument with lower spectral resolution such as FLEX offers much higher spatial resolution.

It is of great importance for the general applicability of the inversion results that the scheme robustly finds the global minimum of the cost function. This is ensured by a large number of random starting values and a comparison of the resulting synthetic SNR value with the prescribed one. If the achieved residual is in the order of the prescribed noise, the inversion is successful and different schemes might only be more efficient in the needed computational burden or memory use. Figure 8 shows the mean inversion signal to noise ratio with respect to spectral resolution, prescribed signal to noise ratio, and the best case and realistic case scenario. The results show clearly that the inversion succeeds and is capable of finding a minimum in the cost function which can be completely explained by noise. This is also highlighted in Fig. 1, where several simulated spectra, inversion results, and resulting residuals are shown for three spectral resolutions. The general inversion residual is within the prescribed noise, which indicates that an improvement above the results presented here is only possible by introducing further measurements or additional prior knowledge. However, such an analysis is beyond the scope of this paper.

As discussed above, the methodology of this study is purely Monte Carlo like and an overview about results for the *best case*, *realistic case*, and spectral resolution is shown in Fig. 9. The top row of subfigures shows the effect of unknown aerosol type

AMTD
6, 10511–10550, 2013

and surface inhomogeneity for constant signal to noise ratio, spectral resolution, and spectral sampling. While the results for the aerosol height retrieval even slightly improve, the retrieval of aerosol optical depth is affected by relaxing these constraints. The aerosol height retrieval is almost unaffected, its bias is slightly reduced and the slope is closer to one. The scatter for aerosol optical depth retrieval increases and the slope deviates more from one. In this respect, the aerosol height retrieval is more stable with respect to aerosol type and surface inhomogeneity than the retrieval of aerosol optical depth. The bottom row of the figure shows the effect of decreasing the spectral resolution and spectral sampling to 0.1 nm. As for the case with higher spectral resolution and sampling, the retrieval of aerosol height is more stable, while the retrieval of aerosol optical depth is more strongly affected.

The presented scatter plots can be seen as an best estimate for a real world validation of a retrieval scheme. Its success can be measured in terms of absolute accuracy, but also relative to given user requirements, which in general strongly depend on a specific application. Aim of this paper is to be rather general and not to base the discussion on a certain user requirement and application. Hence, throughout this paper the absolute retrieval accuracy is taken as measure.

Visible in all scatter plots are minor artifacts which are caused by the grid points of the tabulated aerosol optical depth and aerosol height. The artifacts are horizontal lines of increased occurrence for a parameter value which is a grid point in the lookup table (compare also with Table 1). A real world retrieval could simply avoid these artifacts by using a finer grid in the lookup table, which would then better represent the nonlinear response of the simulations with respect to these parameters. These artifacts are shown in Figs. 9 and 10 to highlight the effects of a finite resolution in the lookup table, but are excluded in the further analysis.

Similar scatter plots, but for a prescribed signal to noise ratio of 250 are shown in Fig. 10. The general distribution of scatter points is much wider than in Fig. 9, although the regression lines are only slightly affected. It will depend on the desired application whether such scatter can be accepted.

AMTD
6, 10511–10550, 2013

In contrast to other shown inversion results, each subfigure of Figs. 9 and 10 is based on the inversion of 10 000 randomly selected state vectors. Its computation on a standard PC with Intel i7-3770 CPU took approximately 30 min (see also the benchmark results in Sect. 4). Each inversion for a single spectrum was repeated 20 times with randomly selected starting values to ensure convergence to the global minimum of the least squares cost function.

The discussed results provide evidence that the retrieval of aerosol height will depend on instrumental parameters like spectral resolution, spectral sampling, and signal to noise ratio, but also on the scene itself. This is included in the discussion by prescribing or removing the aerosol type information and introducing surface inhomogeneities. Results regarding this assumption are shown in Fig. 11, which compiles the inversion success for surface pressure, aerosol optical thickness, and aerosol height. Inversion success was defined as the mean absolute residual for the 90 % best cases in rescaled units as they were used in Figs. 9 and 10. Zero indicates a perfect mean inversion while one indicates that the mean residual is in the order of the maximum of the range of the retrieved quantity. Surface pressure is shown merely as reference, its retrieval success depends almost only on signal to noise error and decreases only slightly with increasing spectral resolution.

The results for aerosol optical depth and aerosol height behave quite differently. While being sensitive to spectral resolution, the inversion success strongly depends on the signal to noise level. The strongest increase for aerosol optical thickness can be seen when decreasing the spectral resolution from 1 nm to 0.1 nm. From that on, only minor improvements in the retrieval can be achieved by increasing the spectral resolution of the instrument. Again, it will depend on user requirements whether a possibly small gain in retrieval accuracy from increasing the spectral resolution is feasible. Similar, but weaker behavior can be seen for the retrieval of aerosol height. Depending on the signal to noise level, the retrieval of aerosol height could become worse for increased spectral resolution. It should be noted, that these results describe the inversion success with respect to spectral resolution at constant signal to noise range. When

AMTD
6, 10511–10550, 2013

increasing the spectral resolution, one automatically increases the dynamic range of the signal since the fine oxygen absorption lines become better and better resolved. While these features carry information about the aerosol height, they are strongly affected by noise, which can lead to a decrease in retrieval accuracy. For a real instrument, increasing the spectral resolution will affect the signal to noise level or other parameters such as spatial resolution.

For the shown results, the *realistic case* background information parameters were used. Figure 12 shows the behavior of the aerosol type and aerosol height with respect to spectral resolution, aerosol type information, and surface inhomogeneity. All combinations of known/unknown aerosol type and homogeneous/inhomogeneous surface are shown. The overall effect is minor and is more pronounced for the aerosol optical thickness. A conclusion is, that the retrieval of aerosol height is robust against variations in aerosol type and surface homogeneity. This conclusion is valid for the total physical space which has been discussed here. It could be exploited in much more detail, e.g. by analyzing it with respect to specific aerosol optical parameters and surface conditions, but is left as subject for future research.

Although beyond the scope of this paper and likely of any aerosol retrieval based purely on the oxygen A band, the presented scheme allows to investigate to what extent possible aerosol type information can be retrieved. Results of such an analysis are shown in Fig. 13, which shows the fraction of correctly retrieved aerosol type with respect to spectral resolution, prescribed signal to noise ratio, and surface inhomogeneity. In general, the fraction of correctly retrieved aerosol type is increasing with increasing spectral resolution and is decreasing with increasing signal to noise ratio and increasing surface inhomogeneity. Although far from being the best approach of retrieving the aerosol type, hyperspectral radiance measurements in the oxygen A band could potentially contribute to a better retrieval of aerosol type.

AMTD
6, 10511–10550, 2013

7 Conclusions

A fast forward operator for the simulation of hyperspectral radiances in the oxygen A band was described, benchmarked on a standard computer, and applied for a sensitivity study concerning the retrieval of aerosol optical depth and aerosol height. Study parameters were spectral resolution, spectral sampling, signal to noise ratio, aerosol type information, and surface inhomogeneity. The study showed that the retrieval generally benefits from higher spectral resolution, with the strongest increase in retrieval accuracy above a spectral resolution of 0.1 nm. Signal to noise ratio strongly affects the retrieval and is a key parameter when designing an instrument and a retrieval scheme. The retrieval of aerosol height seems to be robust even when aerosol type information is missing and when surface inhomogeneity is introduced. These conclusions hold for the retrieval of a single aerosol layer when a single aerosol layer is present. More complex vertical profiles should be subject to future research. Evidence was found that the oxygen A band contains valuable information about the aerosol type, which could be used in an aerosol retrieval which utilizes additional spectral bands. The dependency with respect to the temperature profile was not discussed here and might be subject to future research.

Acknowledgements. We wish to thank our colleague Rasmus Lindstrot for fruitful discussions and for his help when preparing the manuscript.

References

Aiazzi, B., Alparone, L., Barducci, A., Baronti, S., Marcoionni, P., Pippi, I., and Selva, M.: Noise modelling and estimation of hyperspectral data from airborne imaging spectrometers, Ann. Geophys., 49, 1, doi:10.4401/ag-3141, 2006. 10523

Amiridis, V., Tsekeri, A., Marinou, E., Wandinger, U., Kazadzis, S., Giannakaki, E., Mamouri, R., Kokkalis, P., and Herekakis, T.: Lidar Climatology of Vertical Aerosol Structure for Space-Based Lidar Simulation Studies, Final Report, ESA-ESTEC Contract RFQ/3-

AMTD
6, 10511–10550, 2013

13301/11/NL/FF/fk, 2013, available at: http://lidar.space.noa.gr:8080/livas/ (last access: November 2013), 2013. 10513

Amodeo, A., Pappalardo, G., Bösenberg, J., Ansmann, A., Apituley, A., Alados-Arboledas, L., Balis, D., Böckmann, C., Chaikovsky, A., Comeron, A., Freudenthaler, V., Gustaffson, O., Hansen, G., Mitev, V., Nicolae, D., Papayannis, A., Perrone, M., Pietruczuk, A., Pujadas, M., Putaud, J., Ravetta, F., Rizi, V., Simeonov, V., Spinelli, N., Stoyanov, D., Trickl, T., and Wiegner, M.: A European research infrastructure for the aesorol study on a continental scale: EARLINET-ASOS, Proceedings of the SPIE, 6745, 67450Y, doi:10.117/12.738401, 2007. 10513

Andreae, M. O.: Soot carbon and excess fine potassium: long-range transport of combustion-derived aerosols, Science, 220, 1148–1151, doi:10.1126/science.220.4602.1148, 1983. 10512

Bennartz, R. and Fischer, J.: A modified k-distribution approach applied to narrow band water vapour and oxygen absorption estimates in the near infrared, J. Quant. Spectrosc. Ra., 66, 539–553, 2000. 10519

Betzer, P. R., Carder, K. L., Duce, R. A., Merrill, J. T., Tindale, N. W., Uematsu, M., Costello, D. K., Young, R. W., Feely, R. A., Breland, J. A., Bernstein, R. E., and Greco, A. M.: Long-range transport of giant mineral aerosol particles, Nature, 336, 568–571, doi:10.1038/336568a0, 1988. 10512

Bézy, J.-L., Bensi, P., Berger, M., Carnicero, B., Davidson, M., Drinkwater, M., Durand, Y., Héliere, F., Ingmann, P., Langen, J., Lin, C., Meynart, R., Rebhan, H., Silvestrin, P., and Thompson, A.: ESA Future Earth Observation Explorer Missions, Proc. of SPIE, 7081, 70810S, doi:10.1117/12.797159, 2008. 10513

Bösch, H., Toon, G. C., Sen, B., Washenfelder, R. A., Wennberg, P. O., Buchwitz, M., de Beek, R., Burrows, J. P., Crisp, D., Christi, M., Connor, B. J., Natraj, V., and Yung, Y. L.: Space-based near-infrared CO_2 measurements: testing the Orbiting Carbon Observatory retrieval algorithm and validation concept using SCIAMACHY observations over Park Falls, Wisconsin, J. Geophys. Res.-Atmos., 111, D23302, doi:10.1029/2006JD007080, 2006. 10515

Chin, M., Kahn, R. A., and Schwartz, S. E.: CCSP 2009: Atmospheric Aerosol Properties and Climate Impacts, A Report by the US Climate Change Science Program and the Subcommittee on Global Change Research, National Aeronautics and Space Administration, Washington, D.C., USA, 2009. 10512

AMTD
6, 10511–10550, 2013

Clarke, A. D. and Noone, K. J.: Soot in the Arctic snowpack: a cause for perturbations in radiative transfer, Atmos. Environ., 19, 2045–2053, doi:10.1016/0004-6981(85)90113-1, 1985. 10512

Clissold, P.: ESA SP-1313/4 Candidate Earth Explorer Core Missions – Reports for Assessment: FLEX – FLuorescence EXplorer, ESA Communication Production Office, 2008. 10514

Corradini, S. and Cervino, M.: Aerosol extinction coefficient profile retrieval in the oxygen A-band considering multiple scattering atmosphere, Test case: SCIAMACHY nadir simulated measurements, J. Quant. Spectrosc. Ra., 97, 354–380, doi:10.1016/j.jqsrt.2005.05.061, 2006. 10513

Crisp, D. and Johnson, C.: The orbiting carbon observatory mission, Acta Astronaut., 56, 193–197, doi:10.1016/j.actaastro.2004.09.032, 2005. 10513

De Graaf, M., Stammes, P., Torres, O., and Koelemeijer, R.: Absorbing aerosol index: sensitivity analysis, application to GOME and comparison with TOMS, J. Geophys. Res.-Atmos., 110, D01201, doi:10.1029/2004JD005178, 2005. 10513

Dubuisson, P., Frouin, R., Dessailly, D., Duforêt, L., Léon, J.-F., Voss, K., and Antoine, D.: Estimating the altitude of aerosol plumes over the ocean from reflectance ratio measurements in the O_2 A-band, Remote Sens. Environ., 113, 1899–1911, doi:10.1016/j.rse.2009.04.018, 2009. 10513

Duforêt, L., Frouin, R., and Dubuisson, P.: Importance and estimation of aerosol vertical structure in satellite ocean-color remote sensing, Appl. Optics, 46, 1107–1119, 2007. 10512, 10513

ESA: GMES Sentinels 4 And 5 Mission Requirements Traceability Document, issue 1, revision 0, Tech. rep., European Space Research and Technology Centre, available at: http://esamultimedia.esa.int/docs/EarthObservation/S4_5_5p_MRTD_issue_1.0_authorised.pdf (last access: 22 October 2013), 2012. 10513, 10514

Fell, F. and Fischer, J.: Numerical simulation of the light field in the atmosphere-ocean system using the matrix-operator method, J. Quant. Spectrosc. Ra., 69, 351–388, doi:10.1016/S0022-4073(00)00089-3, 2001. 10519

Fischer, J. and Grassl, H.: Detection of cloud-top height from backscattered radiances within the oxygen A band – Part 1: Theoretical study, J. Appl. Meteorol., 30, 1245–1259, 1991. 10513

AMTD
6, 10511–10550, 2013

Frankenberg, C., Butz, A., and Toon, G. C.: Disentangling chlorophyll fluorescence from atmospheric scattering effects in O_2 A-band spectra of reflected sun-light, Geophys. Res. Lett., 38, L03801, doi:10.1029/2010GL045896, 2011. 10515

Frankenberg, C., Hasekamp, O., O'Dell, C., Sanghavi, S., Butz, A., and Worden, J.: Aerosol information content analysis of multi-angle high spectral resolution measurements and its benefit for high accuracy greenhouse gas retrievals, Atmos. Meas. Tech. Discuss., 5, 2857–2885, doi:10.5194/amtd-5-2857-2012, 2012. 10513

Gabella, M., Kisselev, V., and Perona, G.: Retrieval of aerosol profile variations from reflected radiation in the oxygen absorption A band, Appl. Optics, 38, 3190–3195, doi:10.1364/AO.38.003190, 1999. 10513

Haring, R., Pollock, R., Sutin, B. M., and Crisp, D.: The Orbiting Carbon Observatory Instrument Optical Design, Current Developments in Lens Design and Optical Engineering V, 2004. 10513

Harrison, R. M. and Yin, J.: Particulate matter in the atmosphere: which particle properties are important for its effects on health?, Sci. Total. Environ., 249, 85–101, doi:10.1016/S0048-9697(99)00513-6, 2000. 10512

Heidinger, A. K. and Stephens, G. L.: Molecular line absorption in a scattering atmosphere – Part 2: Application to remote sensing in the O_2 A band, J. Atmos. Sci., 57, 1615–1634, doi:10.1175/1520-0469(2000)057<1615:MLAIAS>2.0.CO;2, 2000. 10513

Hollstein, A. and Fischer, J.: Radiative transfer solutions for coupled atmosphere ocean systems using the matrix operator technique, J. Quant. Spectrosc. Ra., 113, 536–548, 2012. 10519

Hollstein, A. and Lindstrot, R.: Fast reconstruction of hyperspectral radiative transfer simulations by using small spectral subsets: application to the oxygen A band, Atmos. Meas. Tech. Discuss., 6, 8339–8370, doi:10.5194/amtd-6-8339-2013, 2013. 10516, 10517, 10520

Joiner, J., Yoshida, Y., Vasilkov, A. P., Yoshida, Y., Corp, L. A., and Middleton, E. M.: First observations of global and seasonal terrestrial chlorophyll fluorescence from space, Biogeosciences, 8, 637–651, doi:10.5194/bg-8-637-2011, 2011. 10515

Kokhanovsky, A. A. and Rozanov, V. V.: The determination of dust cloud altitudes from a satellite using hyperspectral measurements in the gaseous absorption band, Int. J. Remote Sens., 31, 2729–2744, 2010. 10513

Koppers, G. A. A., Jansson, J., and Murtagh, D. P.: Aerosol optical thickness retrieval from GOME data in the oxygen A-band, ERS symposium on space at the service of our environment No3, Florence, Italy, 14 March 1997, 1997. 10513

AMTD
6, 10511–10550, 2013

Levy, R. C., Remer, L. A., and Dubovik, O.: Global aerosol optical properties and application to moderate resolution imaging spectroradiometer aerosol retrieval over land, J. Geophys. Res.-Atmos., 112, D13210, doi:10.1029/2006JD007815, 2007. 10521

Lindstrot, R. and Preusker, R.: On the efficient treatment of temperature profiles for the estimation of atmospheric transmittance under scattering conditions, Atmos. Meas. Tech., 5, 2525–2535, doi:10.5194/amt-5-2525-2012, 2012. 10519

Lohmann, U. and Feichter, J.: Global indirect aerosol effects: a review, Atmos. Chem. Phys., 5, 715–737, doi:10.5194/acp-5-715-2005, 2005. 10512

McClain, C. R.: A decade of satellite ocean color observations, Annual Review of Marine Science, 1, 19–42, doi:10.1146/annurev.marine.010908.163650, 2009. 10512

McConnell, J. R., Edwards, R., Kok, G. L., Flanner, M. G., Zender, C. S., Saltzman, E. S., Banta, J. R., Pasteris, D. R., Carter, M. M., and Kahl, J. D. W.: 20th-century industrial black carbon emissions altered arctic climate forcing, Science, 317, 1381–1384, doi:10.1126/science.1144856, 2007. 10512

McMichael, A., Campbell-Lendrum, D., Corvalán, C., Ebi, K., Githeko, A., Scheraga, J., and Woodward, A.: Climate change and human health, WHO Library Cataloguing-in-Publication Data, 2003. 10512

Meijer, Y., Ingmanna, P., Löscher, A., and the CarbonSat Mission Advisory Group Team: CarbonSat: ESA's Earth Explorer 8 Candidate Mission, Geophys. Res. Abstr., EGU2012-2474-1, EGU General Assembly 2012, Vienna, Austria, 2012. 10514

Moré, J. J., Sorenson, D. C., Garbow, B. S., and Hillstrom, K. E.: The MINPACK project, in: Sources and Development of Mathematical Software, 88–111, 1984. 10522

Muller, J.-P., Preusker, R., Fischer, J., Zuhlke, M., Brockmann, C., and Regner, P.: ALBEDOMAP: MERIS land surface albedo retrieval using data fusion with MODIS BRDF and its validation using contemporaneous EO and in situ data products, Geoscience and Remote Sensing Symposium, 2007, IGARSS 2007, IEEE International, 2404–2407, 2007. 10512

Natraj, V., Jiang, X., lie Shia, R., Huang, X., Margolis, J. S., and Yung, Y. L.: Application of principal component analysis to high spectral resolution radiative transfer: a case study of the band, J. Quant. Spectrosc. Ra., 95, 539–556, doi:10.1016/j.jqsrt.2004.12.024, 2005. 10516

Nel, A.: Air pollution-related illness: effects of particles, Science, 308, 804–806, doi:10.1126/science.1108752, 2005. 10512

AMTD
6, 10511–10550, 2013

Pedregosa, F., Varoquaux, G., Gramfort, A., Michel, V., Thirion, B., Grisel, O., Blondel, M., Prettenhofer, P., Weiss, R., Dubourg, V., Vanderplas, J., Passos, A., Cournapeau, D., Brucher, M., Perrot, M., and Duchesnay, E.: Scikit-learn: machine learning in Python, J. Mach. Learn. Res., 12, 2825–2830, 2011. 10519

Pelletier, B., Frouin, R., and Dubuisson, P.: Retrieval of the aerosol vertical distribution from atmospheric radiance, Proc. SPIE, 7150, 71501R, doi:10.1117/12.806527, 2008. 10513

Pöschl, U.: Atmospheric aerosols: composition, transformation, climate and health effects, Angew. Chem. Int. Edit., 44, 7520–7540, doi:10.1002/anie.200501122, 2005. 10512

Preusker, R. and Lindstrot, R.: Remote sensing of cloud-top pressure using moderately resolved measurements within the oxygen A band – a sensitivity study, J. Appl. Meteorol. Clim., 48, 1562–1574, 2009. 10513

Quijano, A. L., Sokolik, I. N., and Toon, O. B.: Influence of the aerosol vertical distribution on the retrievals of aerosol optical depth from satellite radiance measurements, Geophys. Res. Lett., 27, 3457–3460, 2000. 10512

Rascher, U., Gioli, B., and Miglietta, F.: FLEX – Fluorescence Explorer: a remote sensing approach to quantify spatio-temporal variations of photosynthetic efficiency from space, in: Photosynthesis, Energy from the Sun, edited by: Allen, J. F., Gantt, E., Golbeck, J. H., and Osmond, B., 1388–1390, Springer Netherlands, doi:10.1007/978-1-4020-6709-9_299, 2008. 10514

Rodgers, C. D.: Inverse Methods for Athmospheric Sounding, World Scientific Publishing Co. Pte. Ltd., 2000. 10514

Rosen, J. M., Hofmann, D. J., and Laby, J.: Stratospheric aerosol measurements II: The worldwide distribution, J. Atmos. Sci., 32, 1457–1462, doi:10.1175/1520-0469(1975)032<1457:SAMITW>2.0.CO;2, 1975. 10513

Rothman, L., Gordon, I., Barbe, A., Benner, D., Bernath, P., Birk, M., Boudon, V., Brown, L., Campargue, A., Champion, J.-P., Chance, K., Coudert, L., Dana, V., Devi, V., Fally, S., Flaud, J.-M., Gamache, R., Goldman, A., Jacquemart, D., Kleiner, I., Lacome, N., Lafferty, W., Mandin, J.-Y., Massie, S., Mikhailenko, S., Miller, C., Moazzen-Ahmadi, N., Naumenko, O., Nikitin, A., Orphal, J., Perevalov, V., Perrin, A., Predoi-Cross, A., Rinsland, C., Rotger, M., Simecková, M., Smith, M., Sung, K., Tashkun, S., Tennyson, J., Toth, R., Vandaele, A., and Auwera, J. V.: The HITRAN 2008 molecular spectroscopic database, J. Quant. Spectrosc. Ra., 110, 533–572, doi:10.1016/j.jqsrt.2009.02.013, 2009. 10519

AMTD
6, 10511–10550, 2013

Rozanov, V. V. and Kokhanovsky, A. A.: Semianalytical cloud retrieval algorithm as applied to the cloud top altitude and the cloud geometrical thickness determination from top-of-atmosphere reflectance measurements in the oxygen A band, J. Geophys. Res.-Atmos., 109, D05202, doi:10.1029/2003JD004104, 2004. 10513

Sanders, A. F. J. and de Haan, J. F.: Retrieval of aerosol parameters from the oxygen A band in the presence of chlorophyll fluorescence, Atmos. Meas. Tech., 6, 2725–2740, doi:10.5194/amt-6-2725-2013, 2013. 10514, 10521, 10524

Sanghavi, S., Martonchik, J. V., Landgraf, J., and Platt, U.: Retrieval of the optical depth and vertical distribution of particulate scatterers in the atmosphere using O_2 A- and B-band SCIAMACHY observations over Kanpur: a case study, Atmos. Meas. Tech., 5, 1099–1119, doi:10.5194/amt-5-1099-2012, 2012. 10513

Seaton, A., Godden, D., MacNee, W., and Donaldson, K.: Particulate air pollution and acute health effects, The Lancet, 345, 176–178, doi:10.1016/S0140-6736(95)90173-6, 1995. 10512

Stoll, M.: The FLEX – Fluorescence Explorer mission project: motivations and present status of preparatory activities, Geoscience and Remote Sensing Symposium, 2003, IGARSS '03, Proceedings, 2003 IEEE International, 1, 585–587, 2003. 10514

Torres, O., Bhartia, P., Herman, J., Ahmad, Z., and Gleason, J.: Derivation of aerosol properties from satellite measurements of backscattered ultraviolet radiation: theoretical basis, J. Geophys. Res.-Atmos., 103, 17099–17110, 1998. 10513

Veefkind, J., Aben, I., McMullan, K., Förster, H., de Vries, J., Otter, G., Claas, J., Eskes, H., de Haan, J., Kleipool, Q., van Weele, M., Hasekamp, O., Hoogeveen, R., Landgraf, J., Snel, R., Tol, P., Ingmann, P., Voors, R., Kruizinga, B., Vink, R., Visser, H., and Levelt, P.: TROPOMI on the ESA Sentinel-5 Precursor: a {GMES} mission for global observations of the atmospheric composition for climate, air quality and ozone layer applications, Remote Sens. Environ., 120, 70–83, doi:10.1016/j.rse.2011.09.027, 2012. 10513, 10514

Velazco, V. A., Buchwitz, M., Bovensmann, H., Reuter, M., Schneising, O., Heymann, J., Krings, T., Gerilowski, K., and Burrows, J. P.: Towards space based verification of CO_2 emissions from strong localized sources: fossil fuel power plant emissions as seen by a CarbonSat constellation, Atmos. Meas. Tech., 4, 2809–2822, doi:10.5194/amt-4-2809-2011, 2011. 10514

AMTD
6, 10511–10550, 2013

Winker, D. M., Vaughan, M. A., Omar, A., Hu, Y., Powell, K. A., Liu, Z., Hunt, W. H., and Young, S. A.: Overview of the CALIPSO mission and CALIOP data processing algorithms, J. Atmos. Ocean. Tech., 26, 2310–2323, doi:10.1175/2009JTECHA1281.1, 2009. 10513

Winker, D. M., Pelon, J., Coakley, J. A., Ackerman, S. A., Charlson, R. J., Colarco, P. R., Flamant, P., Fu, Q., Hoff, R. M., Kittaka, C., Kubar, T. L., Le Treut, H., McCormick, M. P., Mégie, G., Poole, L., Powell, K., Trepte, C., Vaughan, M. A., and Wielicki, B. A.: The CALIPSO mission: a global 3-D view of aerosols and clouds, B. Am. Meteorol. Soc., 91, 1211–1229, doi:10.1175/2010BAMS3009.1, 2010. 10513

Wiscombe, W. J.: Improved Mie scattering algorithms, Appl. Optics, 19, 1505–1509, 1980. 10521

Zieger, P., Ruhtz, T., Preusker, R., and Fischer, J.: Dual-aureole and sun spectrometer system for airborne measurements of aerosol optical properties, Appl. Optics, 46, 8542–8552, 2007. 10513

AMTD
6, 10511–10550, 2013

Table 1. Parameter grid of the lookup table. The table contains 4·5·3·5·2·2·13·8·20 = 2 496 000 states and corresponding spectra.

surface pressure ρ	$n_\rho = 4$	ρ = 800 hPa, 950 hPa, 1013 hPa, 1050 hPa
aerosol optical thickness	$n_\tau = 5$	$\tau = 0.0, 0.3, 0.6, 0.9, 1.2$
aerosol center height	$n_h = 3$	h = 500 m, 2500 m, 4500 m
aerosol type	$n_t = 5$	$t = 1, 2, 3, 4, 5$ (dust, urban, continental, neutral, absorbing)
surface reflectance at 755 nm	$n_{\alpha_1} = 2$	$\alpha_1 = 0.1, 0.7$
surface reflectance at 780 nm	$n_{\alpha_2} = 2$	$\alpha_2 = 0.1, 0.7$
viewing zenith angle μ	$n_\mu = 13$	μ = 0.00, 7.44, 13.63, 19.76, 25.88, 31.99, 38.10, 44.21, 50.32, 56.42, 62.53, 68.63, 74.74 in °
solar zenith angle μ_S	$n_{\mu_S} = 8$	μ_S = 0.00, 7.44, 13.63, 19.76, 25.88, 31.99, 38.10, 44.21 in °
relative azimuth angle ϕ	$n_\phi = 20$	ϕ = 0.00, 9.47, 18.95, 28.42, 37.89, 47.37, 56.84, 66.32, 75.79, 85.26, 94.74, 104.21, 113.68, 123.16, 132.63, 142.11, 151.58, 161.05, 170.53, 180.00 in °

AMTD
6, 10511–10550, 2013

Table 2. Benchmark results of the fast forward operator on an Intel i7-3770 with respect to the number of used principal components n_P, spectral resolution SR, spectral sampling SS, and for the pure interpolation result $\boldsymbol{y}$ and the interpolations result and corresponding Jacobean $\boldsymbol{y}, \nabla\boldsymbol{y}$. Spectral resolution and spectral sampling were chosen to be the same per run and carry the unit of nm. The unit for the benchmark results is spectra s^{-1}. Eight threads were used for the multithread run.

		single thread		multi thread	
SR = SS	n_P	$\boldsymbol{y}$	$\boldsymbol{y}, \nabla\boldsymbol{y}$	$\boldsymbol{y}$	$\boldsymbol{y}, \nabla\boldsymbol{y}$
0.1	5	5780	1580	26694	7213
0.01	5	5777	1574	26734	7221
0.001	5	5768	1581	26694	7222
0.1	15	4129	845	20100	4072
0.01	15	4125	845	19997	4089
0.001	15	4120	844	20141	4105
0.1	30	3020	500	14213	2325
0.01	30	2974	497	13862	2343
0.001	30	3002	501	13866	2402

AMTD
6, 10511–10550, 2013

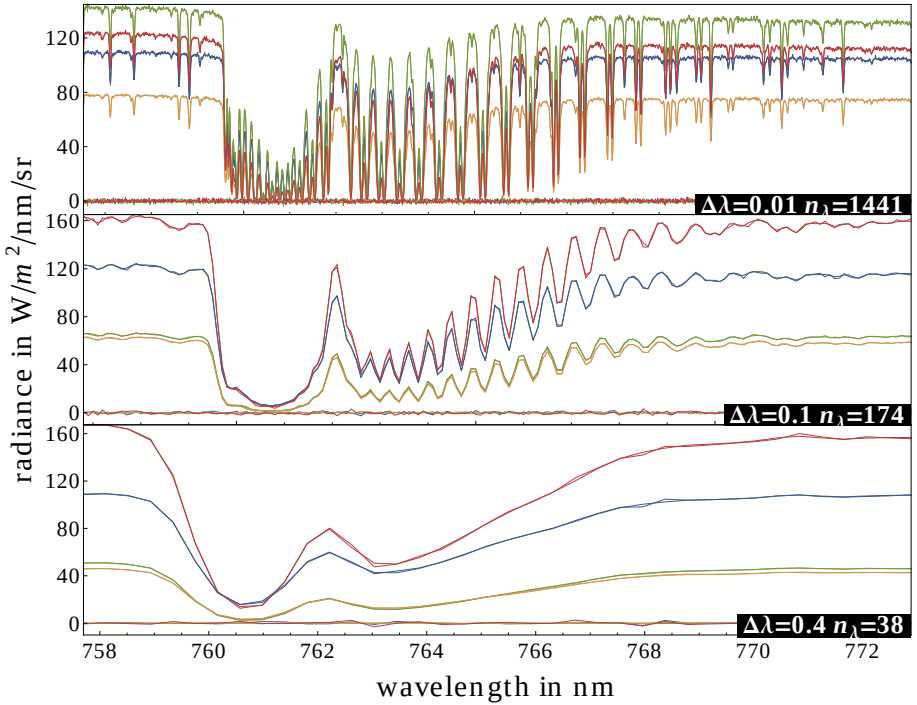

Fig. 1. Random selection of synthetic spectra and inversion results for spectral resolution and sampling of 0.01 nm, 0.1 nm, and 0.4 nm. The synthetic signal to noise ratio was set to 100 (see Sect. 5 for a definition of the noise model) and the thin lines around the zero line show the fit residual.

AMTD
6, 10511–10550, 2013

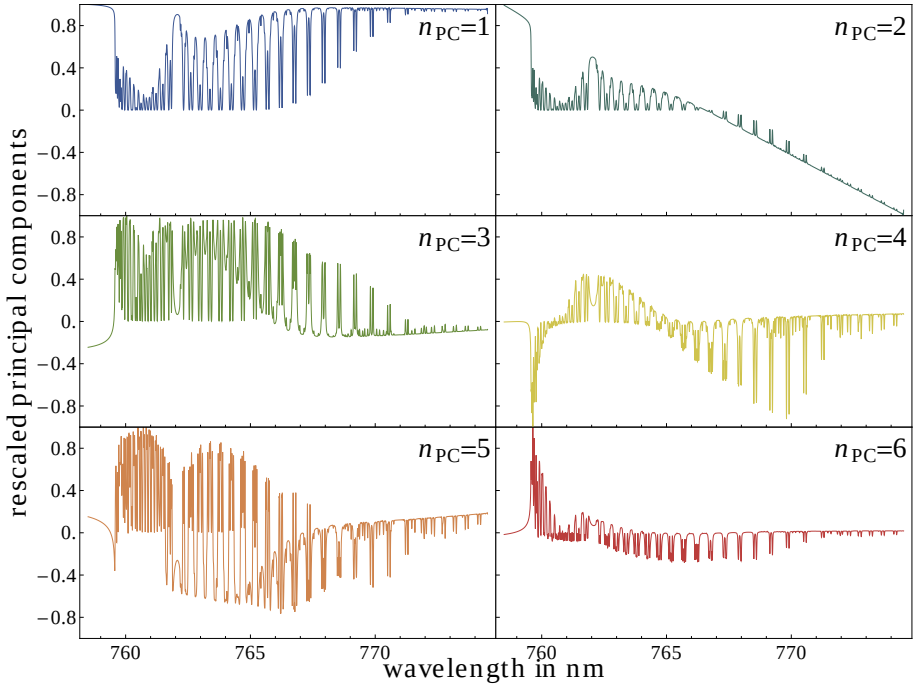

Fig. 2. The first six principal components of the principal component matrix $\mathbf{P}_{n_P}$. The spectra are normalized for better graphical representation.

AMTD
6, 10511–10550, 2013

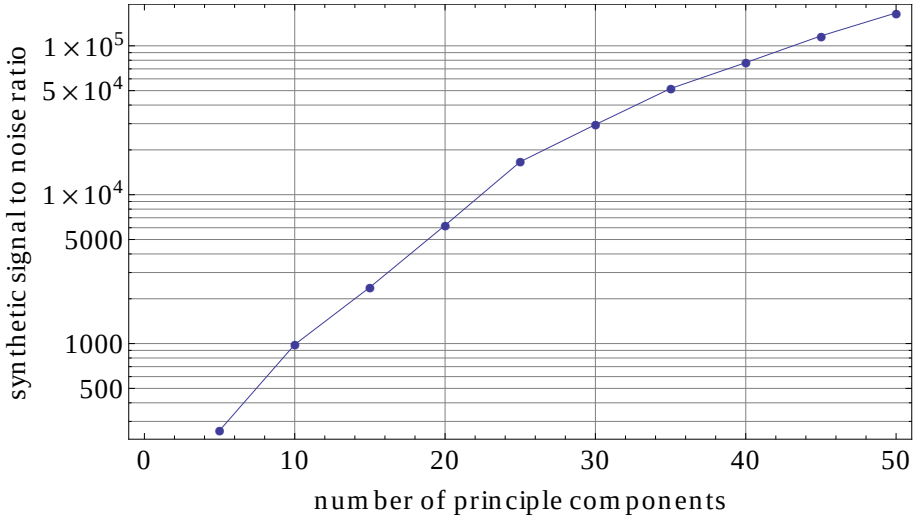

Fig. 3. Mean synthetic SNR with respect to the number n_P of principal components.

AMTD
6, 10511–10550, 2013

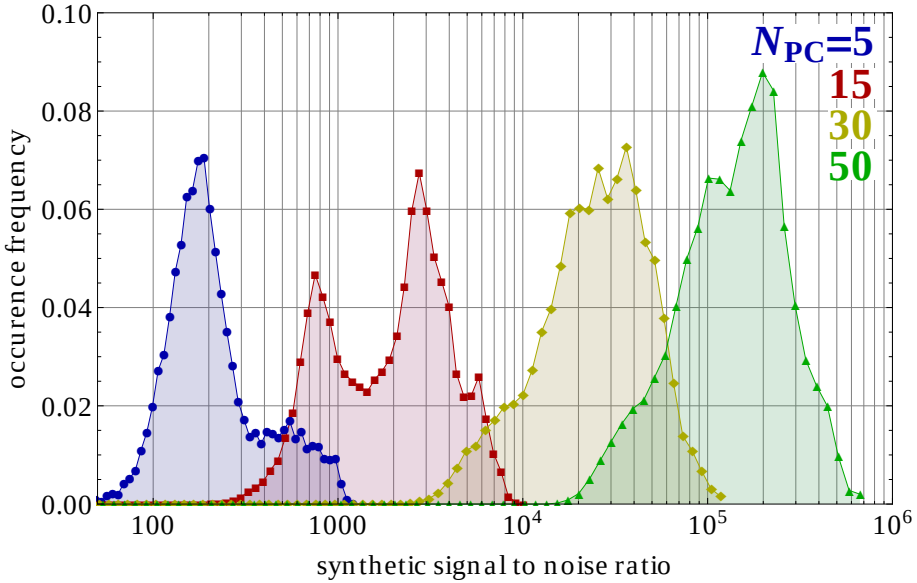

Fig. 4. Histograms of the synthetic SNR for selected values of n_P. Note that the abscissa is in log scale and that occurrence bins were chosen to be equally spaced in a log plot.

AMTD
6, 10511–10550, 2013

Aerosol height retrieval from oxygen A band

A. Hollstein and J. Fischer

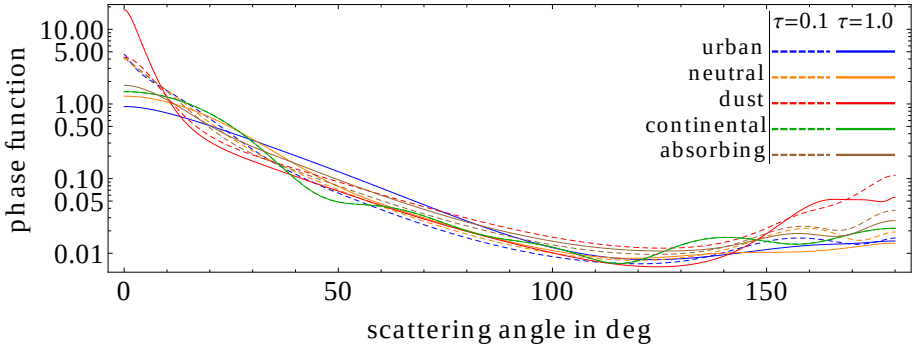

Fig. 5. Phase functions at 774.5 nm of the five used aerosol models.

AMTD
6, 10511–10550, 2013

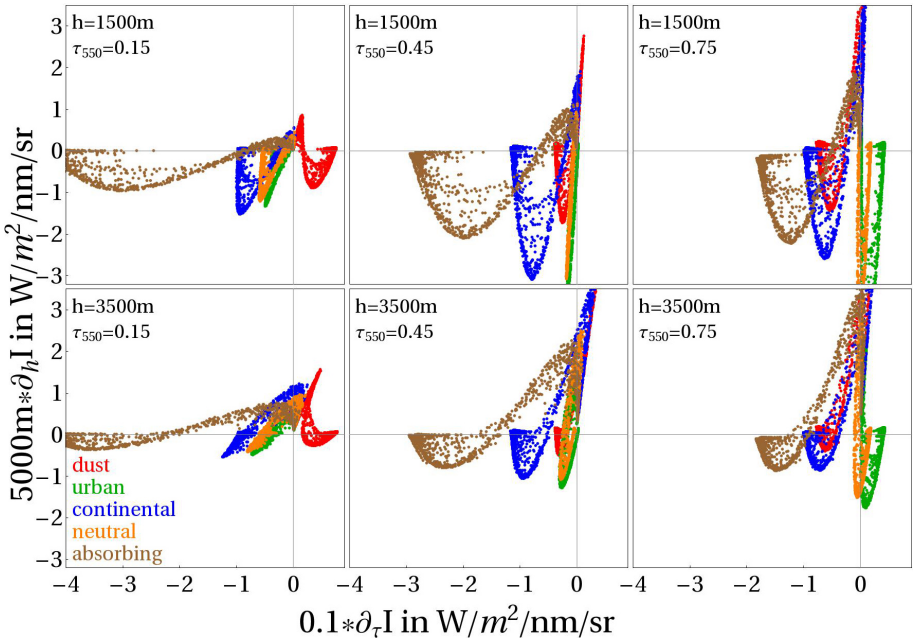

Fig. 6. Several scatter plots of the partial derivative of the fast forward operator with respect to aerosol height and aerosol optical thickness. Both partial derivatives were scaled with a specific decimal power with appropriate unit, such that the unit of the resulting quantity is radiance and that both spectra have similar magnitude. Shown in the top left of each panel is the base aerosol optical thickness and aerosol height. Different colors indicate results for the different aerosol types. From the left to right panel, the aerosol height is kept constant and the aerosol optical thickness increases, while from top to bottom panel the aerosol height is changing. The baseline parameters are, solar angle $\mu_S = 10^\circ$, viewing angle $\mu = 20^\circ$, relative azimuth angle $\varphi = 30^\circ$, surface reflectance is $\alpha = 0.2$, and surface pressure was set to $\rho = 1013$ hPa.

AMTD
6, 10511–10550, 2013

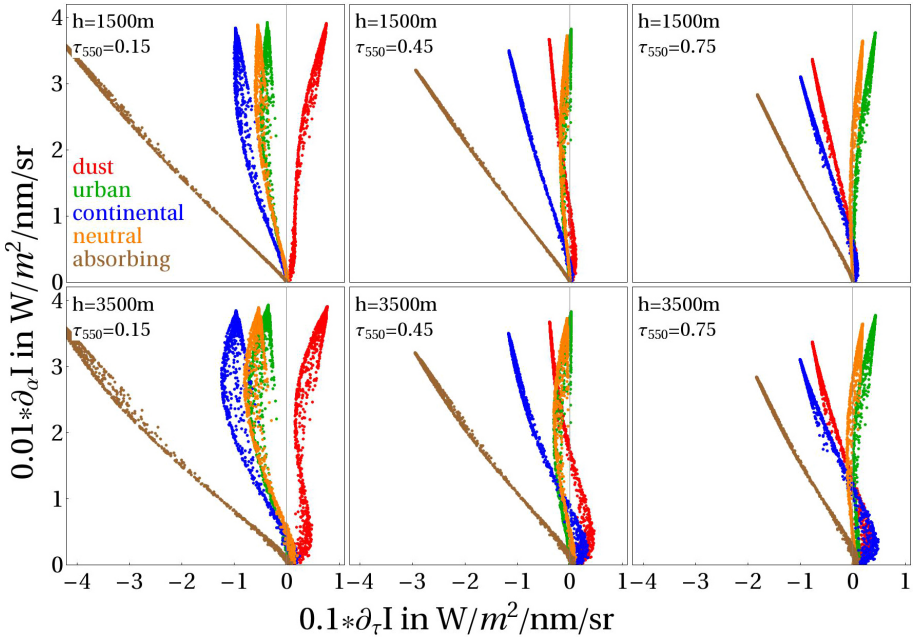

Fig. 7. Similar setup as shown in Fig. 7, but the partial derivatives with respect to surface reflectivity and aerosol optical thickness are compared.

AMTD
6, 10511–10550, 2013

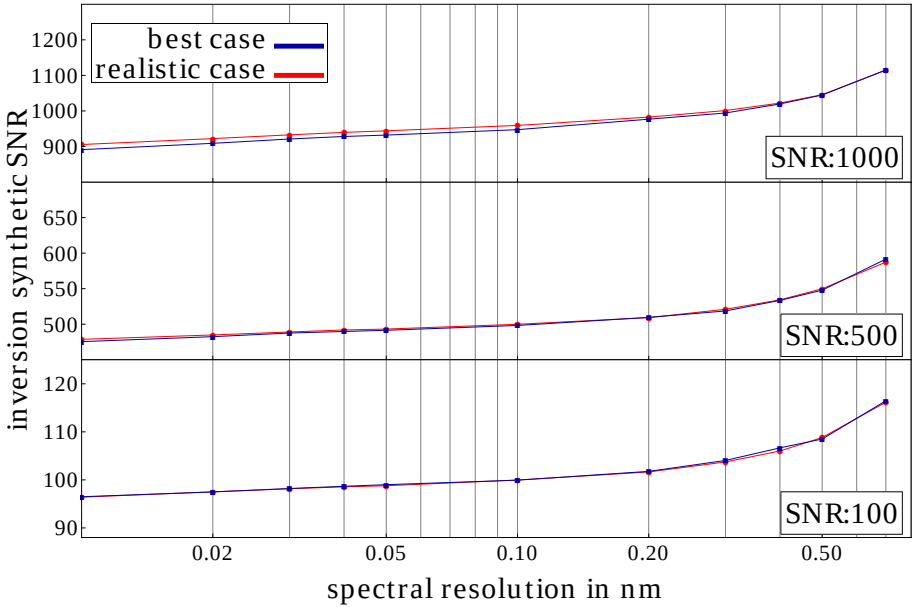

Fig. 8. Mean synthetic signal to noise level from inversion attempts vs. spectral resolution for three prescribed SNR levels. Blue lines indicate the best case setup, whereas results for the realistic case are shown using red color. Spectral sampling is equal to the spectral resolution. The *best case* is characterized by a homogeneous surface and known aerosol model, where the *realistic case* is characterized by an unknown aerosol model and a heterogeneous surface reflectivity.

AMTD
6, 10511–10550, 2013

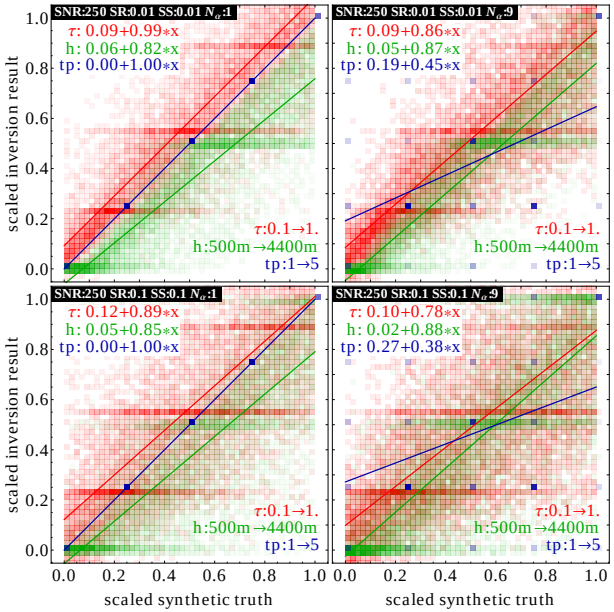

Fig. 9. Overview about inversion runs for various scenarios. Each figure is a combined scatter plot of a retrieved and prescribed parameter for 10 000 randomly selected cases. A scenario is defined by signal to noise level, spectral width, spectral sampling, number of surface reflectances, and aerosol type background information. These background settings are shown in the top left of each figure. Also in the top left shown are line parameters for a linear fit per parameter and the true parameter interval is shown in the bottom right. Shown are retrieval results for the aerosol optical thickness (red), aerosol height (green), and aerosol type (blue). The left column shows results for the the *best case* (aerosol type information known, homogeneous surface with $N_\alpha = 1$) and the right column for the *realistic case* (unknown aerosol type, inhomogeneous surface with $N_\alpha = 9$) scenario. From top to bottom the spectral resolution (SR) and sampling (SS) is decreased from 0.01 nm (top) to 0.1 nm (bottom). The color scale follows an inverse power distribution to enhance the visibility of low density bins.

AMTD
6, 10511–10550, 2013

Aerosol height retrieval from oxygen A band

A. Hollstein and J. Fischer

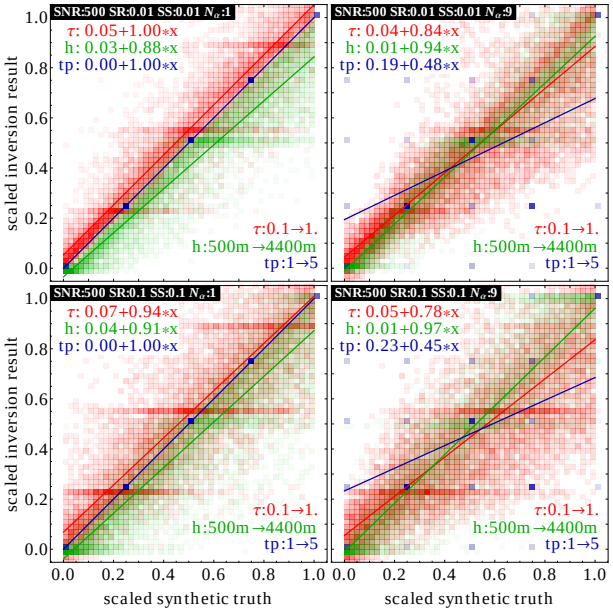

Fig. 10. Similar as Fig. 9, but for a prescribed signal to noise ratio of 250.

AMTD
6, 10511–10550, 2013

Aerosol height retrieval from oxygen A band

A. Hollstein and J. Fischer

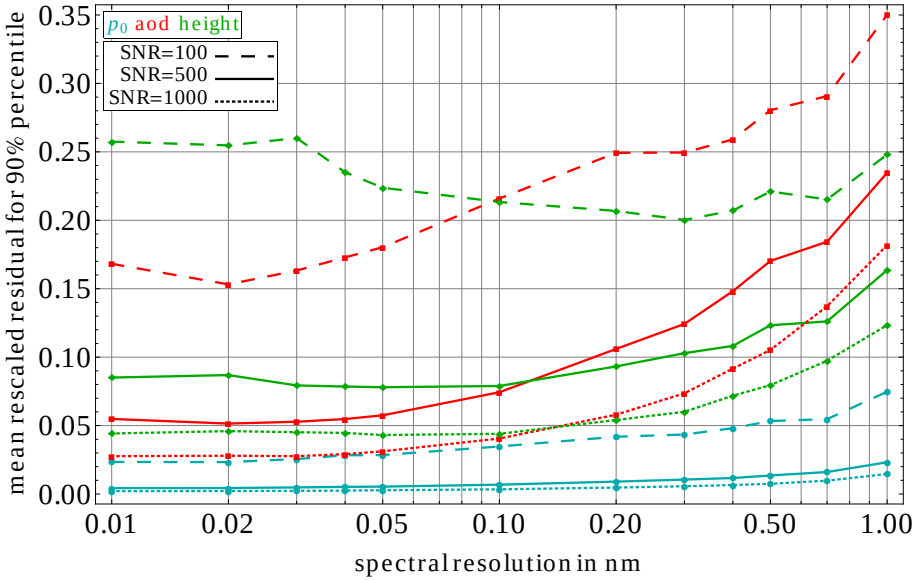

Fig. 11. Inversion success of surface pressure (cyan), aerosol optical depth (red), and aerosol height (green) with respect to spectral resolution and prescribed signal to noise ratio (dashed, solid, dot dashed). Shown is the mean absolute residual of the 90% best inversion results in rescaled units (compare with Figs. 9 and 10). Spectral sampling for each point is equal to spectral resolution. The *realistic case* background settings were used.

AMTD
6, 10511–10550, 2013

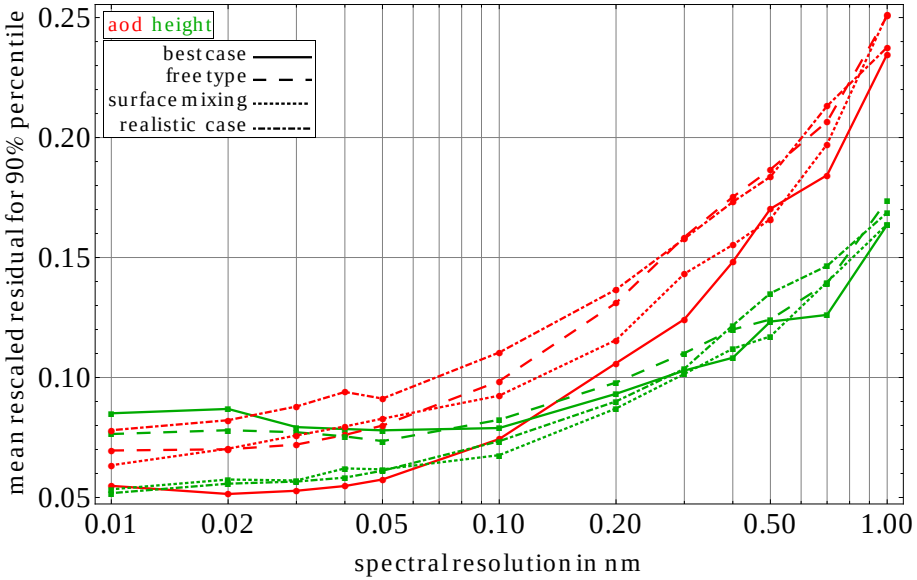

Fig. 12. Similar as Fig. 11 but only for aerosol optical thickness and aerosol height, but with respect to aerosol type information and surface inhomogeneity. Shown are the *best case* and the *realistic case* scenario and also the *free type* scenario where the aerosol type is unknown to the retrieval but the surface is homogeneous and also the *surface mixing* scenario where the aerosol type information is given but the surface is assumed to be inhomogeneous.

AMTD
6, 10511–10550, 2013

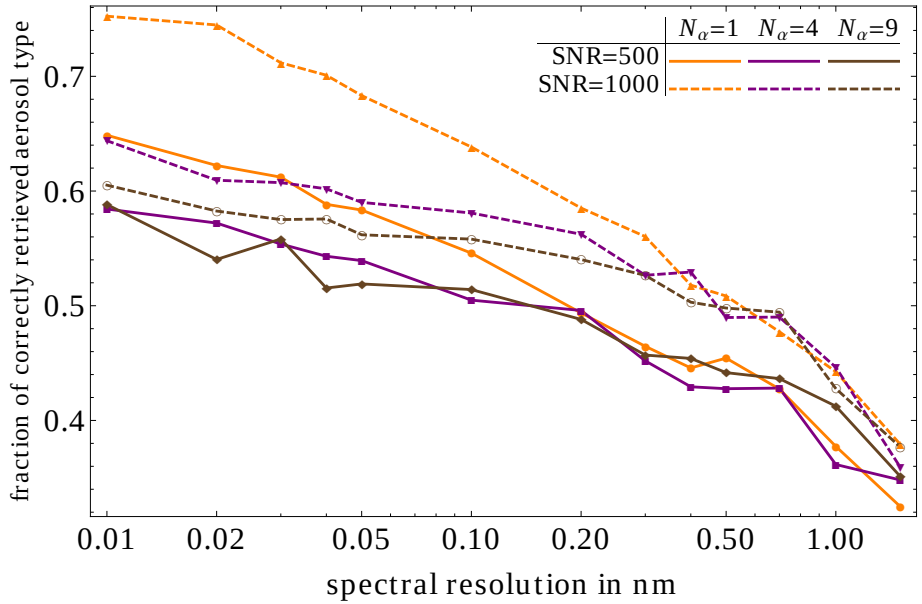

Fig. 13. Fraction of correctly retrieved aerosol type with respect to spectral resolution, prescribed signal to noise ratio (solid/dashed lines), and surface inhomogeneity (red, blue, green color).

AMTD
6, 10511–10550, 2013